nature materials

ARTICLES

PUBLISHED ONLINE: 8 MAY 2017 | DOI: 10.1038/NMAT4898

Dynamic chemical expansion of thin-film non-stoichiometric oxides at extreme temperatures

Jessica G. Swallow[1,2], Jae Jin Kim[1,2], John M. Maloney[1], Di Chen[1,2], James F. Smith[3], Sean R. Bishop[1,2], Harry L. Tuller[1,2] and Krystyn J. Van Vliet[1,2]*

Actuator operation in increasingly extreme and remote conditions requires materials that reliably sense and actuate at elevated temperatures, and over a range of gas environments. Design of such materials will rely on high-temperature, high-resolution approaches for characterizing material actuation *in situ*. Here, we demonstrate a novel type of high-temperature, low-voltage electromechanical oxide actuator based on the model material $Pr_xCe_{1-x}O_{2-\delta}$ (PCO). Chemical strain and interfacial stress resulted from electrochemically pumping oxygen into or out of PCO films, leading to measurable film volume changes due to chemical expansion. At 650 °C, nanometre-scale displacement and strain of >0.1% were achieved with electrical bias values <0.1 V, low compared to piezoelectrically driven actuators, with strain amplified fivefold by stress-induced structural deflection. This *operando* measurement of films 'breathing' at second-scale temporal resolution also enabled detailed identification of the controlling kinetics of this response, and can be extended to other electrochemomechanically coupled oxide films at extreme temperatures.

Materials that enable mechanical actuation and sensing in extreme environments are in high demand for applications including nuclear power control systems[1], jet turbine engines[2], and space exploration[3]. The artificial muscles required of these devices (for example, electric motors and piezoelectrics) are often limited by material microstructural or compositional instability at high temperatures (>200 °C)[4,5]. Further, design of new materials to operate in such extreme environments is limited by lack of direct, high-temperature, high-resolution characterization of actuation. Here, we demonstrate the functionality of non-stoichiometric oxide thin films as a new class of high-temperature, non-volatile and low-voltage electromechanical actuator, using $Pr_xCe_{1-x}O_{2-\delta}$ (PCO) as a model system. PCO, like many non-stoichiometric oxides, exhibits chemical expansion, or a coupling between material volume and composition, at temperatures >500 °C that relate to elevated oxygen vacancy concentrations[6]. This oxide expansion at high temperatures can be enhanced at low oxygen partial pressures, or as demonstrated herein by electrochemical pumping of oxygen vacancies with an applied electrical bias. For films adhered to substrates, the resulting chemically driven strain and associated interfacial stress can induce both volume change in the film and structural deflection of the system.

To quantify this film 'breathing' and deflection due to reversible oxygen uptake within PCO thin films, we employed a distinct probe-based approach (Fig. 1) capable of nanometre-scale displacement and sub-second-scale temporal resolution at temperatures up to 650 °C. In this method, a film of up to micrometre-scale thickness is electrically biased with modest voltages (~100 mV) to drive oxygen content changes within the entire film by adjusting the Nernst electrochemical potential[7–9]. An instrumented but non-conductive displacement probe placed in contact with the film concurrently measures the mechanical response to the applied bias. This approach has several key advantages over existing techniques to measure film expansion by detecting changes in curvature[10], diffraction[11–15], volume[16], or scanning probe electrodes[17–19], particularly at the high temperatures (well over 200 °C) and low electrical biases (well below 1 V) of interest herein; see Supplementary Section 1. This decoupling of electrical bias and mechanical displacement enabled demonstration of nanoscale electrochemomechanical spectroscopy (NECS) on a model high-temperature oxide actuator under conditions characteristic of extreme operating environments, to quantify mechanisms controlling the extent and rate of device actuation.

The model film material of interest is $Pr_{0.1}Ce_{0.9}O_{2-\delta}$ (abbreviated as PCO, where δ indicates non-stoichiometry), a functional oxide that exhibits large strain coupling to δ and has been extensively characterized by a detailed defect model relating temperature and effective p_{O_2} (refs 8,16,20). In PCO, chemical expansion arises largely from an increase in ionic radius of cations during the following reduction reaction, written using Kröger–Vink notation[16,21]:

$$2Pr_{Ce}^{x} + O_{O}^{x} \leftrightarrow 2Pr_{Ce}^{'} + V_{O}^{\bullet\bullet} + \frac{1}{2}O_2(g) \quad (1)$$

where Pr_{Ce}^{x} and $Pr_{Ce}^{'}$ respectively denote Pr^{+4} and Pr^{+3} on Ce^{+4} sites, and O_{O}^{x} and $V_{O}^{\bullet\bullet}$ respectively denote an oxide ion (neutral with respect to the lattice) and an oxide ion vacancy (double positively charged with respect to the lattice) at an oxygen site. We have demonstrated previously that in thin films supported on ionically conducting substrates, this equilibrium can be controlled both by changing the surrounding atmosphere and by application of electrical bias[7,22]. The corresponding strain ε arising from the change in non-stoichiometry $\Delta\delta$ is analogous to thermal expansion; this can be defined as:

$$\varepsilon = \alpha_c \Delta\delta \quad (2)$$

where the unitless chemical-expansion coefficient α_c is 0.087 for PCO (ref. 16). Film adherence to the yttria-stabilized zirconia (YSZ) substrate constrains in-plane chemical strain to produce interfa-

[1]Department of Materials Science and Engineering, Massachusetts Institute of Technology, Cambridge, Massachusetts 02139, USA. [2]Materials Processing Center, Massachusetts Institute of Technology, Cambridge, Massachusetts 02139, USA. [3]Micro Materials Ltd., Wrexham LL13 7YL, UK.
*e-mail: krystyn@mit.edu

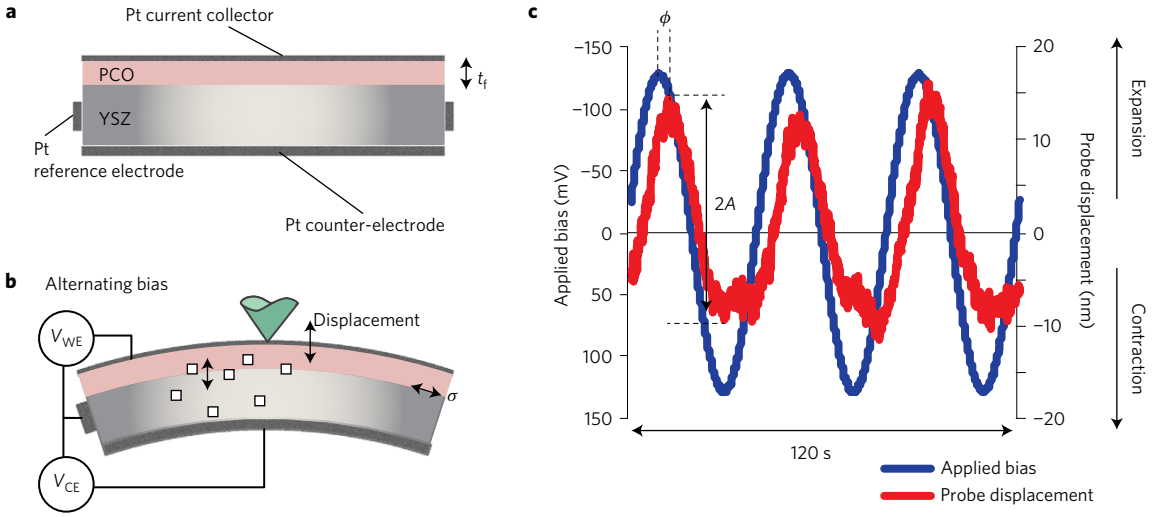

Figure 1 | Dynamic chemical expansion upon oscillating electrical bias. a, Films of $Pr_{0.1}Ce_{0.9}O_{2-\delta}$ (PCO) with deposited thickness t_f ranging from 300 to 1,000 nm were grown on yttria-stabilized zirconia (YSZ) single-crystal substrates (1 mm thickness) with porous Pt reference and counter-electrodes. **b**, The depth-sensing probe rests in contact with the PCO sample surface, with the sample maintained at a constant temperature ranging from 550 to 650 °C. Alternating bias V_{WE} applied to the working electrode with respect to the reference electrode modulates the oxygen activity in the PCO film, causing oxygen vacancies (empty squares) to be pumped in and out of the film through the YSZ substrate. This in turn leads to a mechanical response that is the result of a combination of film volume change and substrate deflection due to PCO chemical expansion, detectable through the probe displacement. **c**, Sinusoidal applied bias (blue) induces a corresponding and lagging change in probe position (red), from which phase lag ϕ and amplitude A are detected. Positive probe displacement indicates increased film thickness (expansion) and positive substrate curvature and is driven by negative (reducing) bias, whereas negative displacement indicates decreased film thickness (contraction) and negative substrate curvature that is driven by positive (oxidizing) bias.

cial stress that can be sufficient to induce detectable deflection. Figure 1 summarizes the film configuration and measurement of NECS at constant elevated temperature. PCO films of varying thickness (~300 to 1,000 nm) and approximately 8 × 8 mm in-plane dimensions on YSZ single-crystal substrates were fabricated with a three-electrode configuration (Fig. 1a; see Methods). Control samples lacking only the PCO film were also prepared to decouple the response of the film from that of the substrate and Pt electrodes, and one PCO/YSZ sample with smaller in-plane film dimensions (3 mm diameter) was prepared to decouple out-of-plane strain from deflection.

During mechanical measurements, a position-sensing probe was placed in contact with the film surface as a sinusoidal electrical bias was applied to the working electrode with respect to the reference electrode (Fig. 1b), and the mechanical displacement was detected as a combination of film thickness change and substrate deflection. Figure 1c shows example traces, illustrating that positive applied bias causes negative probe displacement as the film contracts, while a reduction in bias produces concomitant, reversible film expansion and positive probe displacement. This oxide film contraction under positive bias is expected from the higher effective oxygen partial pressure $p_{O_{2,eff}}$ in the film given by the Nernst relation:

$$p_{O_{2,eff}} = p_{O_{2,g}} \exp[4qE/kT] \quad (3)$$

where E is the applied electrical bias, $p_{O_{2,g}}$ is the ambient oxygen partial pressure, q is the elementary charge, k is the Boltzmann constant, and T is the temperature. The asymmetry in magnitude of mechanical response apparent in Fig. 1c is also reasonably explained by the asymmetry in defect concentration change with respect to applied bias: PCO tends towards stoichiometry ($\delta \to 0$) under more oxidizing conditions and towards $\delta = 0.05$ for more reducing conditions. We detected such reversible, nanometre-scale mechanical response, using electrical biasing frequencies ω ranging from 1 to 0.01 Hz. Probe displacement on film-free control samples exposed to oscillatory electrical bias was <1 nm; we thus concluded that there was little to no detectable contribution to the measured mechanical response from dimensional changes in the substrate, counter-electrode, or current collector. Curvature of the film/substrate system was detected by acquiring measurements at multiple surface locations with millimetre-scale lateral spacing relative to the film centre; see Supplementary Section 2 and Supplementary Fig. 1. Therefore, we attribute the dynamic actuation exemplified in Fig. 1b to concurrent increased PCO film thickness and positive substrate curvature due to interfacial stress.

The oscillatory mechanical response may be characterized by a phase lag ϕ and amplitude A by fitting a sinusoidal function to the probe position (Fig. 1c). Given sufficient time to relax following a change in oxygen activity, the sample can equilibrate fully. Accordingly, with decreasing frequency, the amplitude approaches a maximum value (~10 nm), whereas the phase lag approaches zero (Fig. 2a,b). Further, at higher temperatures with concurrent reduction in oxygen transport barriers, the frequency at which the maximum amplitude is reached increases. As mentioned above, we refer to this mechanical characterization of the sample frequency response as NECS, in analogy to electrical admittance spectroscopy, and determine the complex function Y describing the frequency response of the material relative to the applied signal. (See Supplementary Section 4 for a detailed derivation of this transfer function.) The complex function Y can be described by its modulus A and phase lag ϕ (the negative of phase shift φ) using equations (4) and (5), where τ is the characteristic time of the response and D_0 is the equilibrium displacement amplitude for each sample condition[23]:

$$A = \frac{D_0}{\sqrt{(\omega\tau)^2 + 1}} \quad (4)$$

$$\phi = -\varphi = \tan^{-1}(\omega\tau) \quad (5)$$

Figure 2a,b shows that the measured deflection amplitudes and phase lags were described well by equations (4) and (5), except at the highest frequencies (≥0.5 Hz) where phase lag is

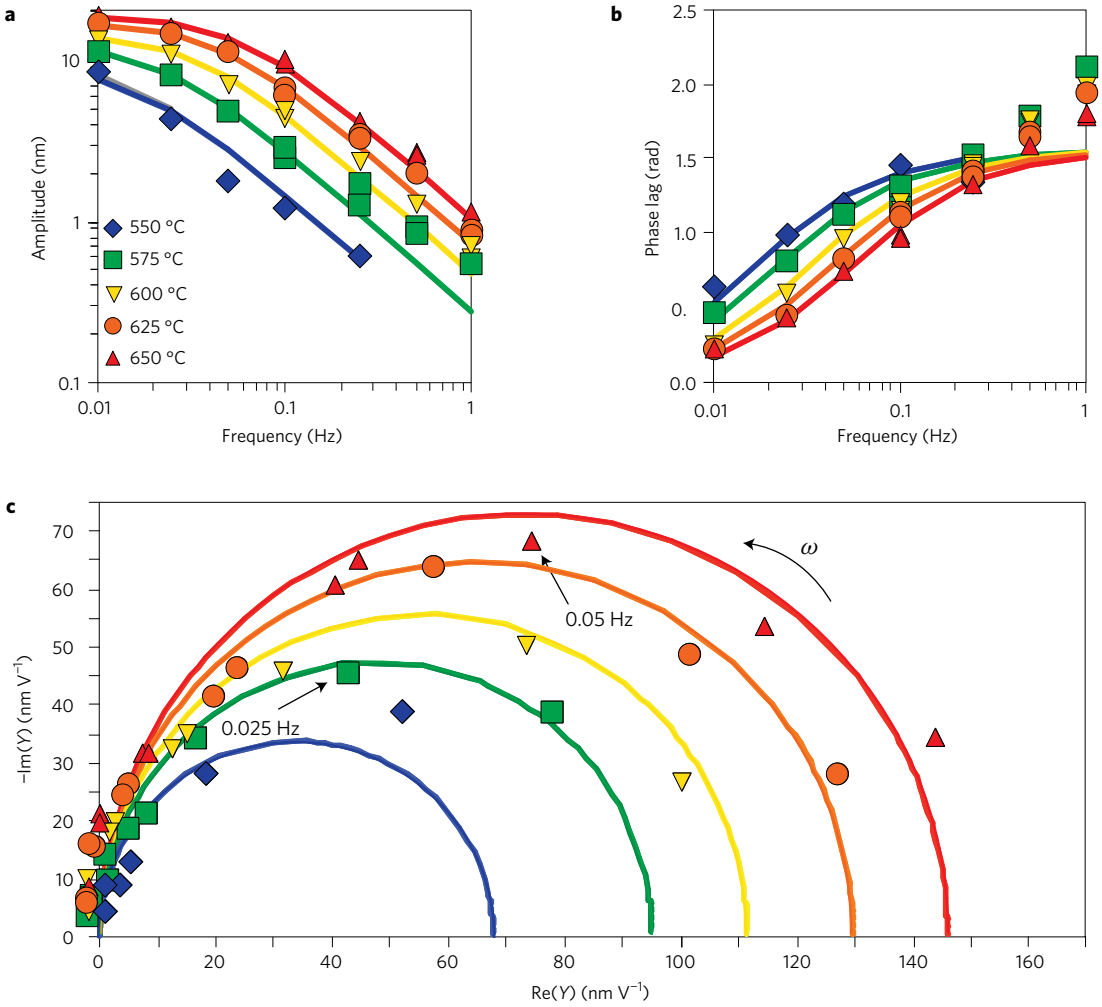

Figure 2 | Sample frequency response to expanding $Pr_{0.1}Ce_{0.9}O_{2-\delta}$ film. a,b, Amplitude A and phase lag ϕ, respectively, obtained at several different temperatures for PCO film thickness of 1 μm. For each temperature, A and ϕ are fitted to a first-order transfer function (solid lines) to estimate the characteristic time and equilibrium (zero-frequency) displacement amplitude D_0 of the mechanical response. With increasing temperature, the expansion response is more rapid, suggesting a temperature-activated process. The discrepancy at higher frequencies between predicted and experimentally obtained phase lag values is discussed in Supplementary Section 5. **c**, Electrochemomechanical admittance Y shown on the complex plane for the same data indicates a single semicircle or process at each temperature. In analogy to electrical admittance spectroscopy, corresponding diameters are equivalent to D_0/E_0, while the frequency at the semicircle maximum marks $\omega\tau = 1$. For all data points, the standard deviation of fitted A or ϕ over ten periods is smaller than the data points.

expected to asymptotically approach π/2 but exceeds this value experimentally. This discrepancy is explained by a slight internal signal collection delay (see Supplementary Section 5). When these data are expressed on the complex plane for a given condition, as in Fig. 2c, the displayed NEC spectrum shows a single characteristic maximum (for example, ~0.05 Hz at 650 °C) corresponding to the characteristic frequency of the sample (where $\omega\tau = 1$). As derived in Supplementary Section 4, the arc diameter in Fig. 2c corresponds to the maximum mechanical displacement D_0, normalized by applied bias amplitude E_0, and τ/D_0 is the inverse rate of displacement. Note that the above relationships and following kinetics analysis are valid even for displacement attributed to concurrent film expansion and substrate curvature.

The capacity to rapidly measure these breathing displacements over a wide range of temperatures and bias-modulated defect contents enables determination of the activation energies E_a indicative of mechanisms by which oxygen moves in and out of functional oxides. Figure 3a shows representative Arrhenius relations from which the activation energies modulating the magnitude of mechanical response D_0 and inverse rate of expansion τ/D_0 for a given sample and condition were determined. These average E_a values were -1.05 ± 0.13 eV (for τ/D_0), and 0.53 ± 0.14 eV (for D_0), reported as mean and standard deviation of at least six measurements across three samples. We also applied conventional *in situ* impedance spectroscopy (IS) to these same sample constructs at 500–700 °C, which allows for separate measurements of activation energies associated with electrical impedance between different working electrodes. We thus determined that the distinct activation energies measured mechanically were consistent with those attributable specifically to the oxygen storage capacity—that is, chemical capacitance—of the PCO film (E_a measured by IS at 0.55 ± 0.07 eV corresponds to displacement magnitude D_0) and to resistance to oxide ion conduction through the YSZ (E_a measured by IS at -0.99 ± 0.06 eV corresponds to inverse displacement rate τ/D_0). These activation energies also agreed well with those reported previously for PCO chemical capacitance [0.6 eV; ref. 24] and YSZ diffusion (1 eV; ref. 25). In accordance with the derivations given for D_0 and τ/D_0 in the Supplementary Information, the good agreement with expected activation energies validated that the calculated maximum breathing displacements D_0 of these oxide films are controlled by

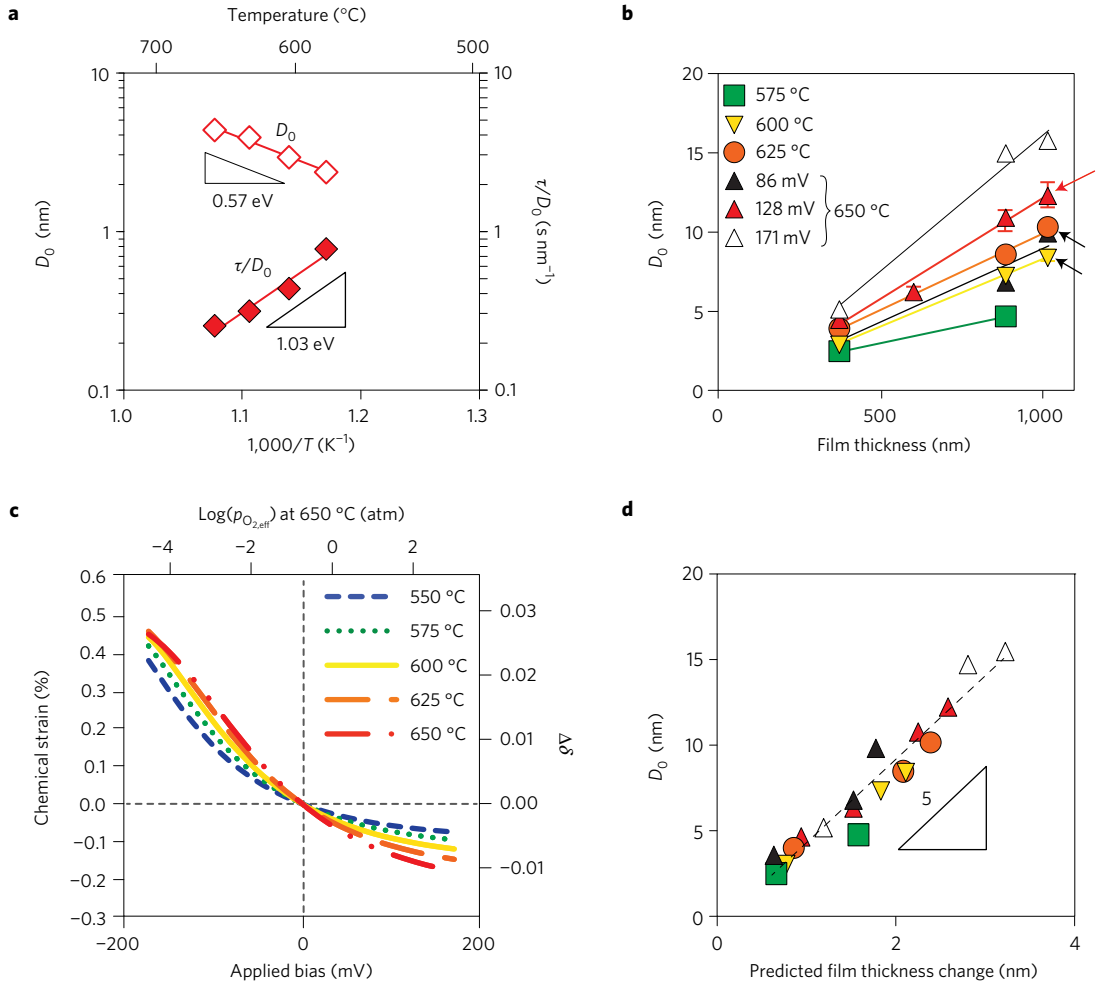

Figure 3 | Factors controlling oxide film breathing. a, Representative Arrhenius plots used to estimate the activation energy for YSZ diffusion and PCO chemical capacitance based on the values of τ/D_0 (inverse deflection rate) and D_0 (deflection magnitude), respectively, identified from the mechanical measurements. These activation energies are comparable to those calculated based on *in situ* impedance spectroscopy. Data shown are for PCO film thickness 371 ± 11 nm. **b**, Equilibrium magnitude D_0 of probe displacement increases with increasing temperature, applied bias amplitude E_0, and film thickness. Data correspond to E_0 of 128 mV unless otherwise noted. Where possible, error bars show the range of measured D_0 values for three replicate measurements. (All films at $E_0 = 128$ mV and $T = 650$ °C, highlighted by a red arrow, and all temperatures with $E_0 = 128$ mV for the film with thickness 1,018 ± 26 nm, highlighted by black arrows.) This range is often smaller than the size of the data points. **c**, Out-of-plane strain ε and non-stoichiometry change $\Delta\delta$ versus applied bias at several temperatures for a constrained PCO thin film as predicted by the defect model for $Pr_{0.1}Ce_{0.9}O_{2-\delta}$ (refs 8,16,20). **d**, Measured deflection amplitude D_0 versus predicted film thickness change based on chemical strains calculated in **c** for the set of measurements shown in **b**. A consistent amplification of 5 ± 0.5 nm nm^{-1} ($\Delta D_0/\Delta\varepsilon$) is observed across all samples, temperatures, and E_0 values, with error determined by bootstrapping as described in Supplementary Section 9.

the chemical capacitance of the thin film PCO, and that the inverse displacement rate τ/D_0 is controlled by the rate of oxygen transport into and out of the PCO film through the YSZ substrate.

Figure 3b shows that D_0 was approximately linear with film thickness t_f, for different temperatures and applied bias amplitudes, with a vertical intercept at $t_f = 0$ of $D_0 \sim \pm 1$ nm similar to that detected for control samples (that is, YSZ substrates with no PCO film). As expected, displacement amplitude increased with increasing temperature at a given applied bias—for example, up to 12 nm at 128 mV and 650 °C for the 1,018 nm film. Further increasing the amplitude of the applied bias from 128 to 171 mV (increasing effective p_{O_2} range by two orders of magnitude) at a constant temperature of 650 °C increased D_0 of that sample up to 16 nm. The observed mechanical response to rapid changes in electrical bias indicates dimensional oscillation in the PCO film that is driven by corresponding changes in oxide ion vacancy content.

To our knowledge, this is the first direct demonstration of such chemical-expansion-driven actuation at high temperatures by oxide films, with tens of nanometres cyclic actuation at hundreds of millivolts applied bias under sustained 650 °C environments. Furthermore, the above measurements are consistent with expectations shown in Fig. 3c from the PCO defect model: PCO is expected to contract upon a combination of decreased oxide ion vacancy and Pr^{3+} ion concentrations (oxidizing condition, positive bias), and vice versa for increased oxide ion vacancy and Pr^{3+} ion concentrations (reducing condition, negative bias)[16,21]. As the film is driven to expand in-plane, interfacial stress can drive substrate deflection at sufficient stress magnitudes and film lateral dimensions. Indeed, curvature was detectable (Supplementary Section 2 and Supplementary Fig. 1) for films of 8 mm in-plane dimensions as used in Figs 1–4, while out-of-plane film expansion of ∼1 nm, but not deflection, was detected for a PCO film of ∼1 μm thickness but significantly smaller lateral dimensions at 650 °C (Supplementary Section 3 and Supplementary Fig. 2). Negative substrate curvature amplifies displacement due to film contraction, while positive substrate curvature amplifies film

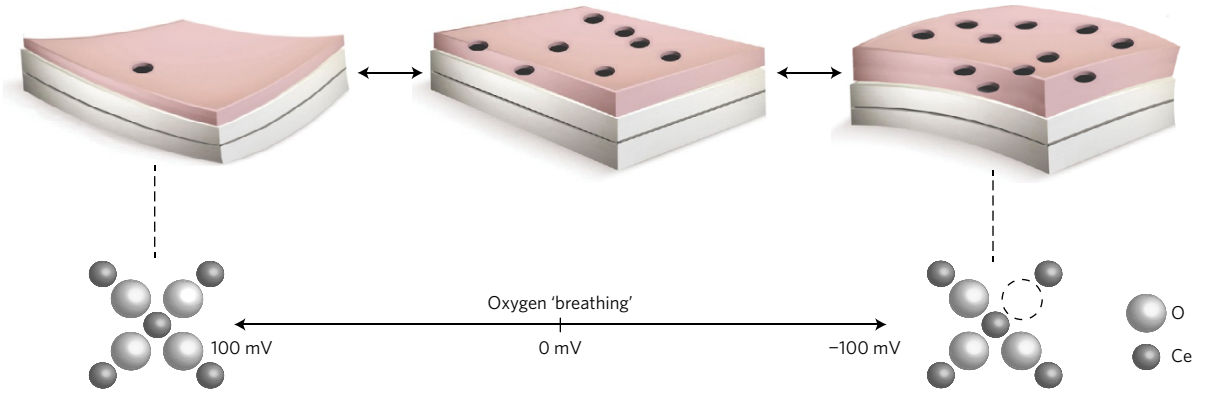

Figure 4 | Schematic of processes occurring during direct chemical-expansion measurement. The film (pink) on an oxide ion conducting substrate (white) is biased with respect to the reference electrode (grey circumscribed perimeter), oscillating between cathodic (negative, reducing) and anodic (positive, oxidizing) conditions. Under anodic bias, the film breathes oxygen in, producing an overall contraction and reduction in film thickness, and corresponding negative substrate deflection. Under cathodic bias, oxygen is released from the film, resulting in increased oxide ion vacancy content (dark holes), a corresponding increase in film thickness, and positive substrate deflection.

expansion. The observed increases in D_0 caused by increased temperature or applied bias amplitude are also reasonable, in that these factors widen the equilibrium boundaries of accessed vacancy concentration, and thus increase the mechanical response. Equilibrium or maximum actuation amplitude is thus proportional to film thickness.

We next consider how chemical strain produced in PCO films subjected to the conditions of this study relates to the displacement amplitude that was observed for all samples. Figure 3c shows that the expected equilibrium strain in these PCO films is 0.2–0.5% (see Supplementary Section 6 for derivation) depending on applied bias and temperature; this estimate also includes a twofold increase in the strain of a constrained film as compared to a freestanding membrane[7,16,22,26]. Figure 3d shows that the detected displacement signal of these PCO–YSZ actuators was consistently amplified over the expected breathing strains as computed in Fig. 3c, by a factor of five. This specific amplification factor is a function of the film lateral dimensions and substrate thickness, and could therefore be tuned accordingly. Additionally, the significant actuation amplitude observed under such extreme environments is repeatable for many cycles and on different samples, and can be tuned further by adjusting film thickness, operating temperature, or applied bias range. The effect described herein for PCO films at temperatures above 500 °C is distinct from the electrostrictive effect described by Lubomirsky *et al.* for Gd-doped cerium oxide (GDC) at temperatures below 200 °C (refs 27,28); those effects in GDC rely on the ordering of vacancies that would not be present at such high temperature, would require much larger electric fields than applied in the present study, and would not be polarity dependent.

Figure 4 summarizes this approach and the findings for PCO films at elevated temperature and dynamically oscillated oxygen content, driven by oscillating anodic and cathodic bias. The approach directly measures displacement, rather than lattice parameter changes, as would be characterized by diffraction, and can be adapted depending on sample design to detect stress-amplified actuation or pure film strain on the scale of nanometres, including at *operando* high temperatures and gas environments. NECS can also be used to estimate changes in activation energy and breathing mechanisms in these or other functional oxide films (for example, battery cathode materials) and multilayers as a function of composition or extreme environment, including the potential for spatially resolved mapping (Supplementary Figs 1 and 2). NECS also provides quantitative insights into the dynamic mechanical response of such materials to electrochemical driving forces, and should facilitate new understanding of materials and conditions that maximize or minimize stress, strain, and fracture under redox cycling or gas interruption for applications in fuel cells, electrolysers, catalysis, or gas sensors, or in response to electrical signals or environmental stimuli for sensor or actuator applications.

Beyond this general methodology to directly measure nanoscale actuation under *operando* conditions, the electrochemically driven breathing response of these specific non-stoichiometric oxide films presents advantages for high-temperature actuation. For example, at a given material thickness of 1 μm, the electrical bias required to produce 0.1% strain is effectively reduced by three orders of magnitude for this PCO system as compared to state-of-the-art high-temperature piezoelectric materials[5] (see Supplementary Section 7); additionally, this actuation is accessible under sustained temperatures far exceeding those at which most piezoelectric actuators operate. Similar to a piezoelectric, the strain response of our system is reversibly proportional to the applied voltage, unlike other electrochemical devices that exhibit more step-wise behaviour from multiple redox reactions[29]. The PCO actuator described herein acts as a model system; there are many chemomechanically coupled non-stoichiometric oxides that could operate according to the same principles[6,9,11]. Furthermore, this design of such actuators has the advantage of non-volatile mechanical memory: if leakage is sufficiently limited (for example, by blocking gas exchange), the device may be 'frozen' in place upon disconnection of the circuit that permits ionic mobility. This opens up a new design space of high-temperature, low-voltage micro-electromechanical systems based on a mechanism that couples electrical signals to mechanical stress and strain via material defect chemistry. Devices based on this alternative actuation mechanism are expected to be of interest in the design of robotics for extreme environments ranging from nuclear power plants to turbine engines to spacecraft.

Methods

Methods, including statements of data availability and any associated accession codes and references, are available in the online version of this paper.

Received 11 September 2015; accepted 3 March 2017; published online 8 May 2017

References

1. Gelhaus, F. E. & Roman, H. T. Robot applications in nuclear power plants. *Prog. Nucl. Energy* **23,** 1–33 (1990).
2. Amrhein, M., Wells, J. & Baudendistel, T. *Design of a High-Temperature Utility Electromechanical Actuator* SAE Technical Paper (SAE International, 2012); http://dx.doi.org/10.4271/2012-01-2214

3. Sherrit, S. Smart material/actuator needs in extreme environments in space. In *Proc. SPIE Smart Structures and Materials 2005: Active Materials: Behavior and Mechanics* Vol. 5761, 335–346 (SPIE, 2005).
4. Damjanovic, D. Materials for high temperature piezoelectric transducers. *Curr. Opin. Solid State Mater. Sci.* **3,** 469–473 (1998).
5. Zhang, S. & Yu, F. Piezoelectric materials for high temperature sensors. *J. Am. Ceram. Soc.* **94,** 3153–3170 (2011).
6. Bishop, S. R. *et al*. Chemical expansion: implications for electrochemical energy storage and conversion devices. *Annu. Rev. Mater. Res.* **44,** 205–239 (2014).
7. Chen, D. & Tuller, H. L. Voltage-controlled nonstoichiometry in oxide thin films: $Pr_{0.1}Ce_{0.9}O_{2-\delta}$ case study. *Adv. Funct. Mater.* **24,** 7638–7644 (2014).
8. Bishop, S. R., Stefanik, T. S. & Tuller, H. L. Electrical conductivity and defect equilibria of $Pr_{0.1}Ce_{0.9}O_{2-\delta}$. *Phys. Chem. Chem. Phys.* **13,** 10165–10173 (2011).
9. Lu, Q. & Yildiz, B. Voltage-controlled topotactic phase transition in thin-film $SrCoO_x$ monitored by *in situ* X-ray diffraction. *Nano Lett.* **16,** 1186–1193 (2016).
10. Sheldon, B. W., Mandowara, S. & Rankin, J. Grain boundary induced compositional stress in nanocrystalline ceria films. *Solid State Ion.* **233,** 38–46 (2013).
11. Hopper, E. M. *et al*. Oxygen exchange in $La_{0.6}Sr_{0.4}Co_{0.2}Fe_{0.8}O_{3-\delta}$ thin-film heterostructures under applied electric potential. *J. Phys. Chem. C* **119,** 19915–19921 (2015).
12. Hiraiwa, C. *et al*. Chemical expansion and change in lattice constant of Y-doped $BaZrO_3$ by hydration/dehydration reaction and final heat-treating temperature. *J. Am. Ceram. Soc.* **96,** 879–884 (2013).
13. Grande, T., Tolchard, J. R. & Selbach, S. M. Anisotropic thermal and chemical expansion in Sr-substituted $LaMnO_{3+\delta}$: implications for chemical strain relaxation. *Chem. Mater.* **24,** 338–345 (2012).
14. Tomkiewicz, A. C., Tamimi, M. A., Huq, A. & McIntosh, S. Evidence for the low oxygen stoichiometry of cubic $Ba_{0.5}Sr_{0.5}Co_{0.5}Fe_{0.5}O_{3-\delta}$ from *in-situ* neutron diffraction. *Solid State Ion.* **253,** 27–31 (2013).
15. McIntosh, S., Vente, J. F., Haije, W. G., Blank, D. H. A. & Bouwmeester, H. J. M. Oxygen stoichiometry and chemical expansion of $Ba_{0.5}Sr_{0.5}Co_{0.8}Fe_{0.2}O_{3-\delta}$ measured by *in situ* neutron diffraction. *Chem. Mater.* **18,** 2187–2193 (2006).
16. Bishop, S. R., Tuller, H. L., Kuru, Y. & Yildiz, B. Chemical expansion of nonstoichiometric $Pr_{0.1}Ce_{0.9}O_{2-\delta}$: correlation with defect equilibrium model. *J. Eur. Ceram. Soc.* **31,** 2351–2356 (2011).
17. Kalinin, S. V. & Balke, N. Local electrochemical functionality in energy storage materials and devices by scanning probe microscopies: status and perspectives. *Adv. Mater.* **22,** E193–E209 (2010).
18. Kumar, A., Ciucci, F., Morozovska, A. N., Kalinin, S. V. & Jesse, S. Measuring oxygen reduction/evolution reactions on the nanoscale. *Nat. Chem.* **3,** 707–713 (2011).
19. Balke, N. *et al*. Nanoscale mapping of ion diffusion in a lithium-ion battery cathode. *Nat. Nanotech.* **5,** 749–754 (2010).
20. Bishop, S. R., Stefanik, T. S. & Tuller, H. L. Defects and transport in $Pr_xCe_{1-x}O_{2-\delta}$: composition trends. *J. Mater. Res.* **27,** 2009–2016 (2012).
21. Marrocchelli, D., Bishop, S. R., Tuller, H. L. & Yildiz, B. Understanding chemical expansion in non-stoichiometric oxides: ceria and zirconia case studies. *Adv. Funct. Mater.* **22,** 1958–1965 (2012).
22. Chen, D., Bishop, S. R. & Tuller, H. L. Non-stoichiometry in oxide thin films: a chemical capacitance study of the praseodymium-cerium oxide system. *Adv. Funct. Mater.* **23,** 2168–2174 (2013).
23. Seborg, D. E., Edgar, T. F., Mellichamp, D. A. & Doyle, F. J. III *Process Dynamics and Control* (John Wiley & Sons, 2011).
24. Chen, D. *Characterization and Control of Non-Stoichiometry in $Pr_{0.1}Ce_{0.9}O_{2-\delta}$ Thin Films: Correlation with SOFC Electrode Performance* PhD thesis, Massachusetts Institute of Technology (2014).
25. Manning, P. S., Sirman, J. D. & Kilner, J. A. Oxygen self-diffusion and surface exchange studies of oxide electrolytes having the fluorite structure. *Solid State Ion.* **93,** 125–132 (1997).
26. Bishop, S. R. *et al*. Impact of size scale on electro-chemo-mechanical coupling properties in MIECs: bulk and thin film $(Pr,Ce)O_{2-\delta}$. *ECS Trans.* **61,** 31–36 (2014).
27. Korobko, R. *et al*. Giant electrostriction in Gd-doped ceria. *Adv. Mater.* **24,** 5857–5861 (2012).
28. Korobko, R. *et al*. *In-situ* extended X-ray absorption fine structure study of electrostriction in Gd doped ceria. *Appl. Phys. Lett.* **106,** 042904 (2015).
29. Cheng, C. & Ngan, A. H. W. Reversible electrochemical actuation of metallic nanohoneycombs induced by pseudocapacitive redox processes. *ACS Nano* **9,** 3984–3995 (2015).

Acknowledgements

This work was supported by the US Department of Energy, Basic Energy Sciences, Division of Materials Science and Engineering under award number DE-SC0002633. J.G.S. acknowledges support from the DOE-SCGF Fellowship Program administered by ORISE-ORAU under contract no. DE-AC05-06OR23100. J.J.K. thanks the Kwanjeong Educational Foundation for fellowship support. The authors acknowledge C. S. Kim for additional sample preparation and F. Frankel for assistance with figure preparation. This work made use of the Shared Experimental Facilities supported in part by the MRSEC Program of the National Science Foundation under award number DMR-1419807.

Author contributions

J.G.S., J.J.K., H.L.T. and K.J.V.V. designed the study. J.G.S. developed the dynamic expansion measurement technique and conducted displacement measurements and data analysis. J.J.K. deposited films and conducted impedance measurements, structural characterization and imaging. S.R.B. developed analysis methods and relationships between impedance and mechanical results. J.M.M. designed LabView signal analysis code for detecting expansion phase lag and amplitude. D.C. contributed to sample design and application of the defect model. J.F.S. contributed to frequency-based measurement experimental design. J.G.S., J.J.K., S.R.B., H.L.T. and K.J.V.V. wrote the manuscript.

Additional information

Supplementary information is available in the online version of the paper. Reprints and permissions information is available online at www.nature.com/reprints. Publisher's note: Springer Nature remains neutral with regard to jurisdictional claims in published maps and institutional affiliations. Correspondence and requests for materials should be addressed to K.J.V.V.

Competing financial interests

The authors declare no competing financial interests.

Methods

Sample fabrication. Films of $Pr_{0.1}Ce_{0.9}O_{2-\delta}$ (PCO) with thicknesses of 371 ± 11, 600 ± 20, 883 ± 13, and 1,018 ± 26 nm were grown by pulsed laser deposition (PLD) on single crystal (100) YSZ substrates (MTI Corporation) of dimensions $10 \times 10 \times 1.0\,mm^3$. Substrates were heated to 500 °C after reaching a base pressure of 8.5×10^{-6} torr, and a dense PCO target was ablated by using a 248 nm wavelength coherent COMPex Pro 205 KrF excimer laser with an 8 Hz laser repetition rate at 400 mJ/pulse. An oxygen partial pressure of 10 mtorr was maintained during both the deposition and cooling steps (5 °C min^{-1}). Post-annealing with a sudden increase in oxygen partial pressure at the deposition temperature in the PLD chamber was not included to avoid severe cracks and delamination caused by rapid changes in film volume. Except in the case of the 600 nm film, which was measured by profilometry, film thickness was measured by scanning electron microscopy of films that were cross-sectioned either by cleaving or focused ion beam (FIB) milling (Helios Nanolab 600 Dual Beam Focused Ion Beam Milling System, FEI). Film crystallographic texture was confirmed by X-ray diffraction (X'Pert Pro MPD PANalytical diffractometer) from 2θ–ω coupled scans of the films, which indicated a highly oriented (100) texture. Film surface roughness (root mean square) and grain size were 1.3 ± 0.2 nm and 20–30 nm, respectively, obtained by atomic force microscopy (Digital Instruments Nanoscope IV, Veeco)[30]. Supplementary Figs 5 and 6 in Supplementary Section 8 provide representative examples of surface roughness and X-ray diffraction data.

Porous Pt layers, as the current collector for the PCO working electrode and as the counter-electrode were prepared by a combination of Pt paste and reactive sputtering on the PCO film and the opposite PCO-free substrate surface, with thicknesses of 83 ± 4 nm and 159 ± 31 nm, respectively (as shown in Fig. 1a). As described in detail previously, PtO_x thin films were first prepared by reactive magnetron sputtering (Kurt J. Lesker) at a d.c. power of 50 W from a two-inch-diameter metal target of 99.99% Pt (ACI Alloys) under controlled argon/oxygen (3/7) atmosphere[31]. Pt paste was applied on the top of the sputtered PtO_x layer, except in the centre area of the PCO working electrode, which was reserved for the mechanical response measurements (that is, the region where the probe tip rested on the film surface). Pt paste was also applied to the outer perimeter of the YSZ substrate to serve as the reference electrode. Then, the samples were annealed at 750 °C in air for 2 h with a heating and cooling rate of 2 °C min^{-1}. During this annealing step, PtO_x was reduced to Pt, resulting in a porous film structure. The sputtered porous Pt layer was used to provide a thin layer with controlled thickness in the area for the mechanical measurement, in addition to enhancing adhesion between the Pt paste and ceramic surfaces. There was no evidence of film delamination, as confirmed by subsequent FIB milling to expose the film/electrolyte interfaces for all samples investigated in this study.

Nanoscale electrochemomechanical spectroscopy measurement. Samples were mounted onto a hot stage by applying high-temperature cement (Omega-bond 600) to the corners of the sample, leaving a gap for gas flow to the counter-electrode. Samples were heated at a rate of 1.6 °C min^{-1} to temperatures 550, 575, 600, 625, and 650 °C, and allowed to reach equilibrium for at least 1 h prior to testing. Samples were then brought into contact with a Berkovich-geometry, cubic boron nitride high-temperature probe using a MicroMaterials NanoTest Vantage instrumented indenter. Information on the stability of the cubic boron nitride (cBN) probe material and the precision of the NanoTest Vantage instrumented indenter is available in Section 10 of the Supplementary Information. Using the ModuLab system (Solartron Analytical) in conjunction with the Potentiostat (PSTAT 1Ms/s) and Frequency Response Analyzer (FRA 1 MHz) module, sinusoidal electrical bias signals with amplitudes of 86, 128, and 171 mV were applied to the working electrode with respect to the reference electrode at frequencies of 0.01, 0.025, 0.05, 0.1, 0.25, 0.5, and 1 Hz. The mechanical response of the sample was measured by displacement of the probe detected by the instrumented indenter resting on the sample surface, with the minimum mechanical load necessary to maintain contact. Each driving frequency was run for a minimum of 35 periods to ensure that the fitting algorithm described in Supplementary Section 9 had measured the parameters of the response signal to suitable accuracy. Detailed discussion of the sensitivity of detected amplitudes and phase lags to experimental variation is available in Supplementary Section 9.

Impedance testing. The asymmetrical cells used for the mechanical measurement as illustrated in Fig. 1a were also investigated by electrochemical impedance spectroscopy (EIS). The EIS measurements were conducted at temperatures between 500 °C and 700 °C in air and covered the frequency range from ~1–10 mHz to 1 MHz with an a.c. amplitude of 20 mV and no d.c. bias using the ModuLab system (Solartron Analytical) described above. The electrode impedance of both the PCO working electrode and the Pt counter-electrode were separately investigated by using a three-electrode cell configuration including a reference electrode. ZView software (Scribner Associates) was used to fit and construct equivalent circuits to analyse the results. The equivalent circuit models used to analyse these samples have been validated previously on PCO/YSZ systems of the same configuration[22].

In addition to the activation energies reported above, impedance spectroscopy also showed that the PCO oxygen gas surface exchange reaction exhibited a considerably higher E_a of 2.22 ± 0.30 eV, and that the area specific resistance at the counter-electrode exhibited $E_a = 1.61 \pm 0.11$ eV.

Data processing and analysis. Input (driving) and output (displacement) signals were collected by a USB-6009 DAQ (National Instruments) and a moving average across each driving cycle was subtracted to remove background noise[32]. Each of the two flattened signals was then fitted by linear least squares to a sum of sine and cosine waves (as described in Supplementary Section 9) to estimate the amplitude and phase lag of the displacement signal relative to the input signal ($V_{input} = A \sin \omega t + B \cos \omega t$, $V_{output} = C \sin \omega t + D \cos \omega t$, where ω is the known driving frequency)[33]. At each experimental condition, oscillatory biasing (with real-time analysis) was conducted until the phase lag converged to within 0.1 radians and the amplitude to within 0.5 nm, typically exceeding 30 cycles.

The measured phase lag ϕ and amplitude A of the final ten cycles of data were averaged for each frequency, and for a given condition (that is, temperature and applied bias) the ϕ versus angular frequency ω relationship was fitted to equation (5) with one time constant τ that was then used to fit the A versus ω results to equation (4) to determine an equilibrium amplitude D_0 at maximum applied bias. The fit was performed using customized Matlab software. These D_0 and τ values were then used to estimate activation energies for the expansion signal, as shown in Fig. 3a, and the fitted value of D_0 was used to estimate equilibrium (zero-frequency) mechanical response and determine the amplification factor. Reported activation energies are the average and standard deviation of at least six measurements across all three samples tested. Detailed discussion of the sensitivity of calculated D_0, τ, E_a, and amplification factor values to experimental and sample-to-sample variation is available in Supplementary Section 9.

Data availability. Source data for Figs 1–3 and example film displacement data are available from the online data repository Figshare with identifier http://dx.doi.org/10.6084/m9.figshare.4681324. Remaining data that support the findings of this study are available from the corresponding author upon reasonable request.

References

30. Kim, J. J., Bishop, S. R., Thompson, N., Kuru, Y. & Tuller, H. L. Optically derived energy band gap states of Pr in ceria. *Solid State Ion.* **225,** 198–200 (2012).
31. Jung, W., Kim, J. J. & Tuller, H. L. Investigation of nanoporous platinum thin films fabricated by reactive sputtering: application as micro-SOFC electrode. *J. Power Sources* **275,** 860–865 (2015).
32. Maloney, J. M., Lehnhardt, E., Long, A. F. & Van Vliet, K. J. Mechanical fluidity of fully suspended biological cells. *Biophys. J.* **105,** 1767–1777 (2013).
33. Kutner, M. H., Nachtsheim, C. J., Neter, J. & Li, W. *Applied Linear Statistical Models* (McGraw-Hill, 2005).